Contents lists available at ScienceDirect

Applied Catalysis B: Environmental

Synthesis and characterization of visible light responsive Bi$_3$NbO$_7$ porous nanosheets photocatalyst

Qingqian Wang, Lupan Yuan, Mei Dun, Xiaomei Yang, Huan Chen, Jinlin Li, Juncheng Hu*

Key Laboratory of Catalysis and Materials Science of the State Ethnic Affairs Commission & Ministry of Education, South-Central University for Nationalities, Wuhan 430074, PR China

A B S T R A C T

Bi$_3$NbO$_7$ single crystal nanosheets have been fabricated through a solvothermal method. The characterization results show that the phase and morphology could be controlled by adjusting reaction parameters such as urea content and pH value. Under appropriate conditions, Bi$_3$NbO$_7$ nanosheets with square pores can be obtained. These novel porous nanosheets are potential photocatalysts with the narrow band gap which allows to utilizing visible light irradiation for photocatalysis. The results of the photocatalytic tests exhibit the porous ones have higher activity than those nonporous ones. After four batches of photodegradation of Rhodanmine B (RhB), the samples still had stable porous structure and no deactivation.

© 2016 Elsevier B.V. All rights reserved.

1. Introduction

With the high development of society and technology, both energy and environmental problems have attracted world-wide attention [1–4]. As one of the most promising ways to solve these problems, semiconductor photocatalysts has been studied much due to their potential application in both solar energy conversion and environment purification, including water splitting [5,6], degradation of harmful organic contaminants [7,8] and reduction of CO$_2$ to organic fuel sources [9]. Various semiconductor photocatalysts have been exploited in the past few years [10,11]. To date, TiO$_2$-based semiconductor photocatalysts has made undoubtedly remarkable progress because of their superb photocatalytic activity and high stability [12,13]. However, its applications are limited by its wide band gap (3.2 eV), which absorbs only UV light (less than 5% of solar light energy). Aiming at developing visible-light-driven photocatalysts, many efforts have been made to efficiently utilize solar energy in photocatalysis field, generally comprising two aspects: One is to improve TiO$_2$ photocatalytic property by modifying technology such as doping [14], sensitization [15], or transition metal loading methods [16], but they often suffer from some new problems such as thermal instability, high recombination rate of electrons and holes, and high costs on metal loading; the other focuses on developing novel visible-light responsive photocatalysts [17].

Recently, a family of niobates and Bi-based oxides has been proved to possess a good visible-light response and exhibit excellent photocatalytic activity. Bismuth-based oxides such as Bi$_2$MoO$_6$, Bi$_2$WO$_6$, BiVO$_4$, *etc* are found to be promising photocatalysts which possess visible light response and exhibit excellent photocatalytic activity [18–20]. The narrow band gap is attributed to the Bi 6s orbitals to the formation of valence band. Niobates contain bismuth have been synthesized and studied in these years. However, niobates were conventionally obtained by solid-state method, which demanded harsh requirement of high temperature (above 1000 °C) and have low visible-light photocatalytic activity because of small specific surface area, and large particle size. Considering these problems, Bi$_3$NbO$_7$ so far has generally obtained by wet-chemical methods since traditional solid-state reaction cannot form the pure phase. For example, Jiang et al. had successfully prepared nanostructured Bi$_3$NbO$_7$ films via an ultrasonic spray pyrolysis way which could be very potential for photoelectrochemical water splitting [21]. Zhang et al. had reported Bi$_3$NbO$_7$ nanoparticles synthesized by the sol-gel method, exhibiting a high visible light photocatalytic activity on degradation of acid red G in water and acetone in air [22]. Wang et al. synthesized cubic Bi$_3$NbO$_7$ nanoparticles through a solvothermal method. These cubic nanoparticles exhibited photocatalytic activity not only to degradation of phenol and aqueous ammonia, but also to evolution hydrogen from water under visible light irradiation [23]. It

* Corresponding author.
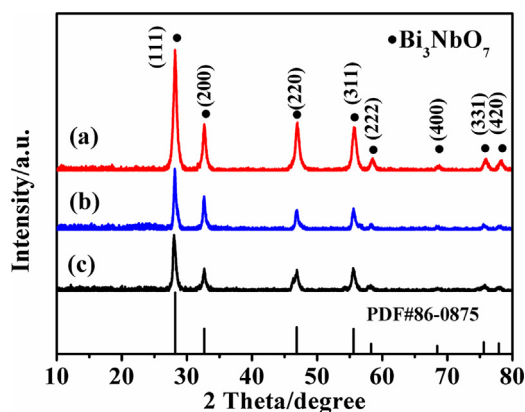 *E-mail address:* jchu@mail.scuec.edu.cn (J. Hu).

Fig. 1. XRD patterns of BNO samples, (a) BNO-3, (b) BNO-2, (c) BNO-1.

Fig. 2. XRD patterns of BNO samples obtained at different pH values, (a) 0.47 (no regulation), (b) pH 7, (c) pH 13 (BNO-3).

is notable that these approaches to bismuth niobates always have some disadvantages such as complex two-stepped synthesis, hazardous solvents like hydrofluoric acid for dissolution, deactivation of Bi_3NbO_7 nanoparticles during the photocatalytic reactions *etc*. Thus, it is very important to develop novel niobates containing bismuth photocatalysts with visible light response.

In this work, Bi_3NbO_7 nanosheets had been successfully synthesized through a simple and direct solvothermal route, with niobium oxalate used as raw material eliminating a complex process of dissolving the niobium sources. Besides, compared with previous study, we prepared porous Bi_3NbO_7 nanosheets with regular pores and conducted detailed analysis on the morphology structure of Bi_3NbO_7 porous nanosheets. The as-prepared Bi_3NbO_7 porous nanosheets possessed higher photocatalytic activity for degradation of RhB and salicylic acid than those nonporous ones.

2. Experimental

2.1. Preparation of Bi_3NbO_7 porous nanosheets

All the reagents were analytical grade and used as received without further purification from Sinopharm Chemical Reagent Co., Ltd. (Shanghai, PR China). In a typical synthesis procedure, 3 mmol of $Bi(NO_3)_3 \cdot 5H_2O$ (1.46 g) was dissolved into 9 mL acetic acid as solution A. Meanwhile, 1 mmol of Niobium oxalate (0.54 g) was added into 40 mL methanol as solution B. Subsequently, solution A was slowly added into solution B in drops under vigorous stirring followed by 20 mL benzyl alcohol, and milky suspension was obtained. Then, 1.68 g urea was added into the mixture and the pH value was adjusted to 13 using potassium hydroxide solution. The suspension was transferred to a 100 mL Teflon-lined stainless autoclave, which was heated to 180 °C for 24 h. After cooled down to ambient temperature naturally, the resulting product was collected and washed with deionized water and ethanol several times, and finally dried at 60 °C for 6 h for further use. The samples were labeled as BNO-1, BNO-2 and BNO-3 with urea content of 0, 0.84 g and 1.68 g respectively in the preparation. As a comparison, bulk Bi_3NbO_7 was synthesized through solid state reaction at 900 for 2 h using Nb_2O_5 and Bi_2O_3 as raw materials and was labeled as BNO-4.

2.2. Characterization of the samples

X-ray diffraction (XRD) patterns were measured on Bruker D8 Advance X-ray diffractometer equipped with a parallel mode and using Cu-Kα radiation (λ = 1.5406 Å) over the 2θ ranging from 10° to 80°. High resolution transmission electron microscopy (HRTEM) was employed to obtain the morphology via a Tecnai G20 (FEI Co., Holland) microscope under the operation conditions of 200 kV,
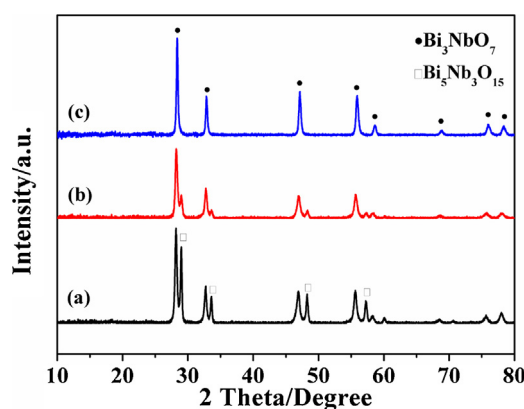
with the sample powder dispersed into ethanol and dropped a very dilute suspension onto a copper grid. The microstructure and composition sizes of the samples were studied by a SU8010 field-emission scanning electron microscope (FESEM, Hitachi, Japan) using 3–5 KV accelerating voltage. The UV–vis diffuse reflectance spectra (DRS) were investigated by Shimadzu UV-2550 spectrophotometer using $BaSO_4$ as a background. X-ray photoelectron spectroscopy (XPS) measurements were carried out on a VG Multilab 2000 (VG Inc.) photoelectron spectrometer taking Al Kα radiation as the excitation source. The Brunauer–Emmett–Teller (BET) specific surface areas of the samples were investigated through the nitrogen adsorption and desorption isotherms with a Micromeritics ASAP 2020 gas adsorption apparatus (USA).

2.3. Photocatalytic tests

The photocatalytic activity of the Bi_3NbO_7 samples was evaluated by the degradation of RhB aqueous solution under visible-light irradiation of a 350 W Xe lamp with a 420 nm cutoff filter. All of the experiments were carried out at room temperature in 100 mL quartz test tubes with reflux water. 50.0 mg catalyst was added into 50.0 mL of RhB (1×10^{-5} mol/L^{-1}) aqueous solution. Then, the solution was treated with ultrasonication for 10 min and stirred for 2 h in darkness. Finally, the results were analyzed by the UV–vis spectrophotometer (UV-2550, Shimadzu).

3. Results and discussion

3.1. XRD patterns

Fig. 1 shows the XRD patterns of different BNO samples. All the peaks of all samples could be indexed to the cubic phase of Bi_3NbO_7 standard XRD data (JCPDS 86-0875) which crystalizes in the space group Fm-3m. The eight peaks could be indexed to (111), (200), (220), (311), (222), (400), (331) and (420) planes at two theta of 28.19°, 32.66°, 46.86°, 55.59°, 58.29°, 68.44°, 75.59° and 77.92° respectively, indicating that this approach could prepare pure Bi_3NbO_7 with no other phase (Fig. 1). The pH value played an important role on the formation of pure phase of Bi_3NbO_7. In Fig. 2, the samples prepared with different pH values were studied and found that if the pH value was not high enough, there would be some $Bi_5Nb_3O_{15}$ synthesized in the final products. The purity of Bi_3NbO_7 increased when the potassium hydroxide solution was added to the system leading to the increase of pH value.
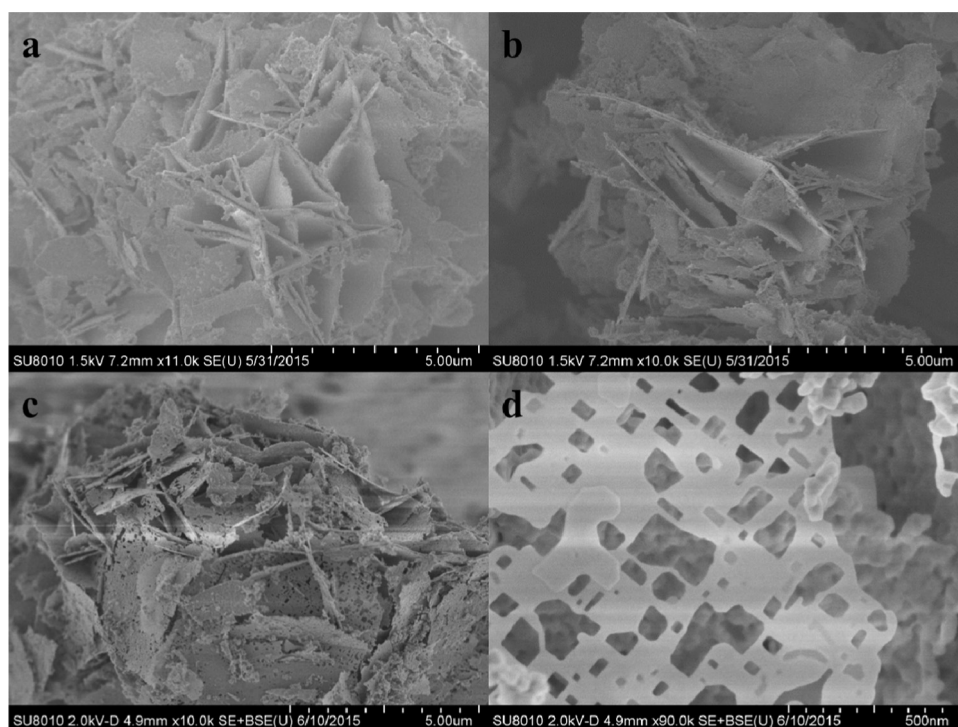
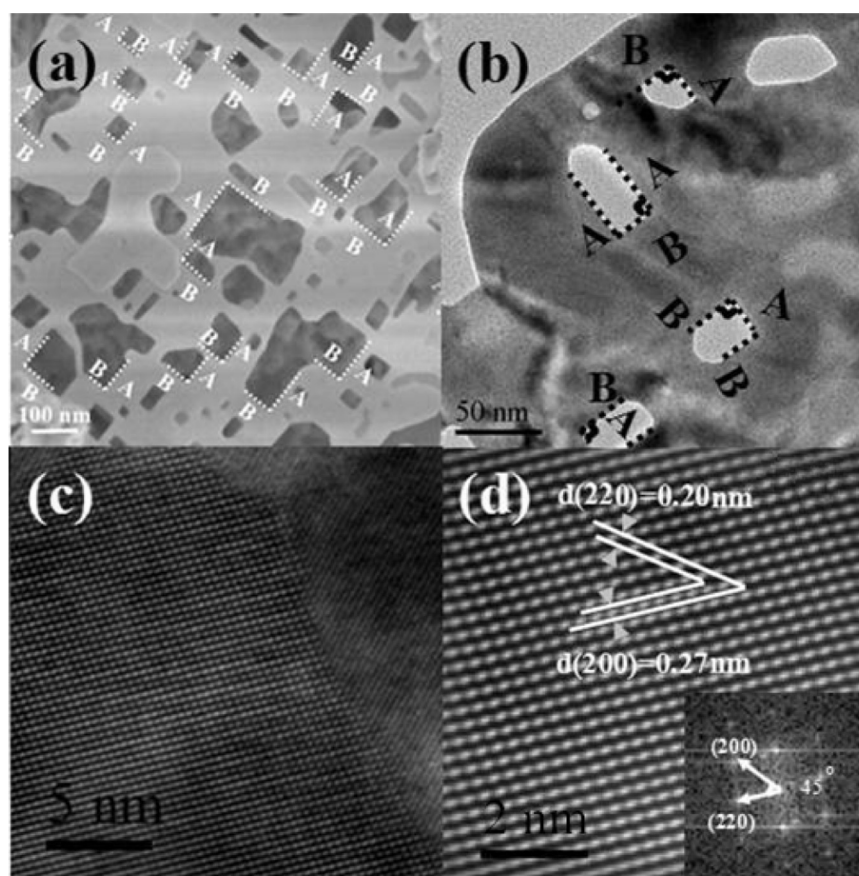**Fig. 3.** SEM images of BNO samples, (a) BNO-1, (b) BNO-2, (c,d) BNO-3.

Fig. 4. SEM and TEM images of Bi_3NbO_7 porous nanosheets (BNO-3), (a) magnified SEM image, (b) low magnification TEM image, (c) magnified TEM image, (d) the corresponding high resolution TEM image and FFT patterns (inset).
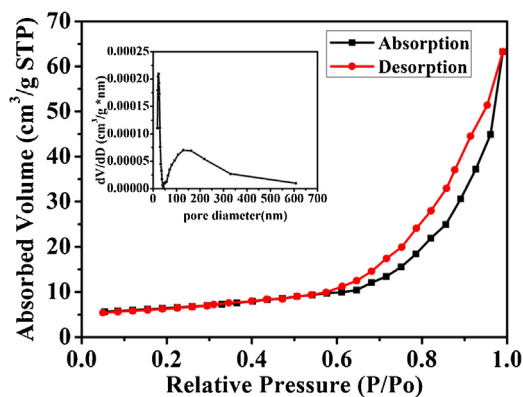
Fig. 5. Nitrogen adsorption–desorption isotherms and pore size distributions (inset) of Bi$_3$NbO$_7$ porous nanosheets (BNO-3).

Fig. 6. UV–vis diffuse reflectance spectra (DRS) of Bi$_3$NbO$_7$ nanosheets, (A) BNO-1, (B) BNO-2, (C) BNO-3.

3.2. Morphology of the BNO samples

The morphology of the BNO samples was investigated by SEM and TEM. As can be seen in Fig. 3, only the sample synthesized with urea content of 1.68 g was porous nanosheets. With the urea content increasing, the pores on the BNO nanosheets became more and more. When the sample was prepared without urea, the nanosheet had little pores (Fig. 3a) and when the urea content was 0.84 g, the pores began to appear on the nanosheet (Fig. 3b). The sample with uniform and porous sheet like structure was formed when 1.68 g urea was added to the fabrication process. The aperture size of the porous nanosheet was ranging from 20 to 200 nm and the average thickness of the nanosheet was about 20 nm (Fig. 3c and d). More detailed information of the porous structure (BNO-3) could
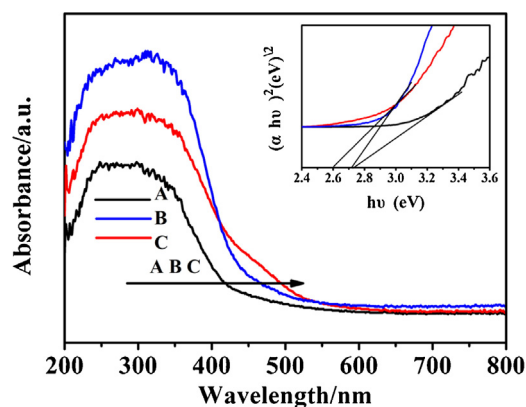
be observed from magnified SEM images and TEM images. In Fig. 4, it was obvious that the pores of the nanosheet were always regular with at least one right angle. Moreover, for an individual nanosheet, the two edges of the right angle were parallel to each other respectively, edge A was parallel to edge A, edge B was parallel to edge B and edge A was perpendicular to edge B for all the regular pores of the nanosheet (Fig. 4a and b). The high resolution TEM images confirmed the order lattice fringes of BNO-3 with an interplanar spacing of 2.0 Å and 2.7 Å, which could be indexed as the (220) and (200) planes of cubic Bi$_3$NbO$_7$ respectively (Fig. 4c and d). The selected area electron diffraction (inset in Fig. 4d) exhibited that the nanosheet was single crystal and the marked angle of (220) and (200) planes was 45°, which was well matched with the the-
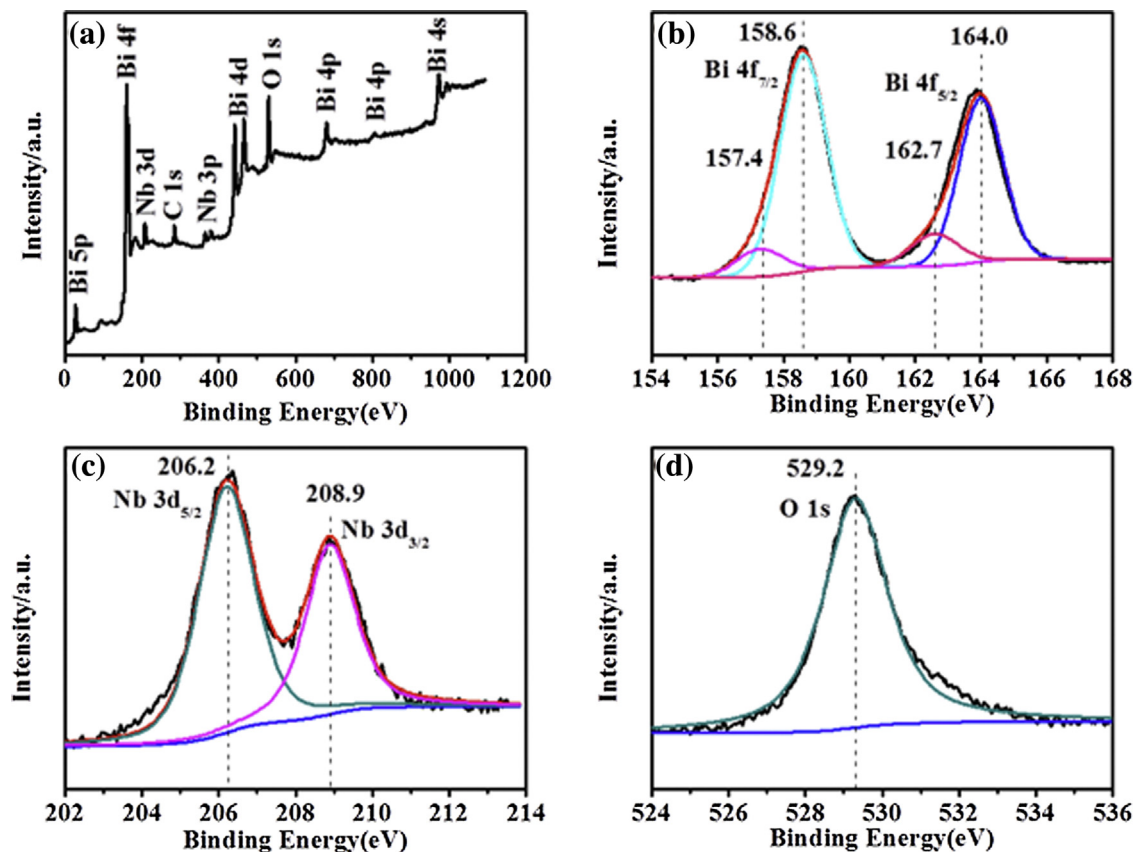

Fig. 7. XPS spectra of the Bi$_3$NbO$_7$ porous nanosheets (BNO-3): (a) XPS survey pattern of the sample, (b) XPS spectrum of the Bi 4f, (c) XPS spectrum of the Nb 3d, (d) XPS spectrum of the O 1s.
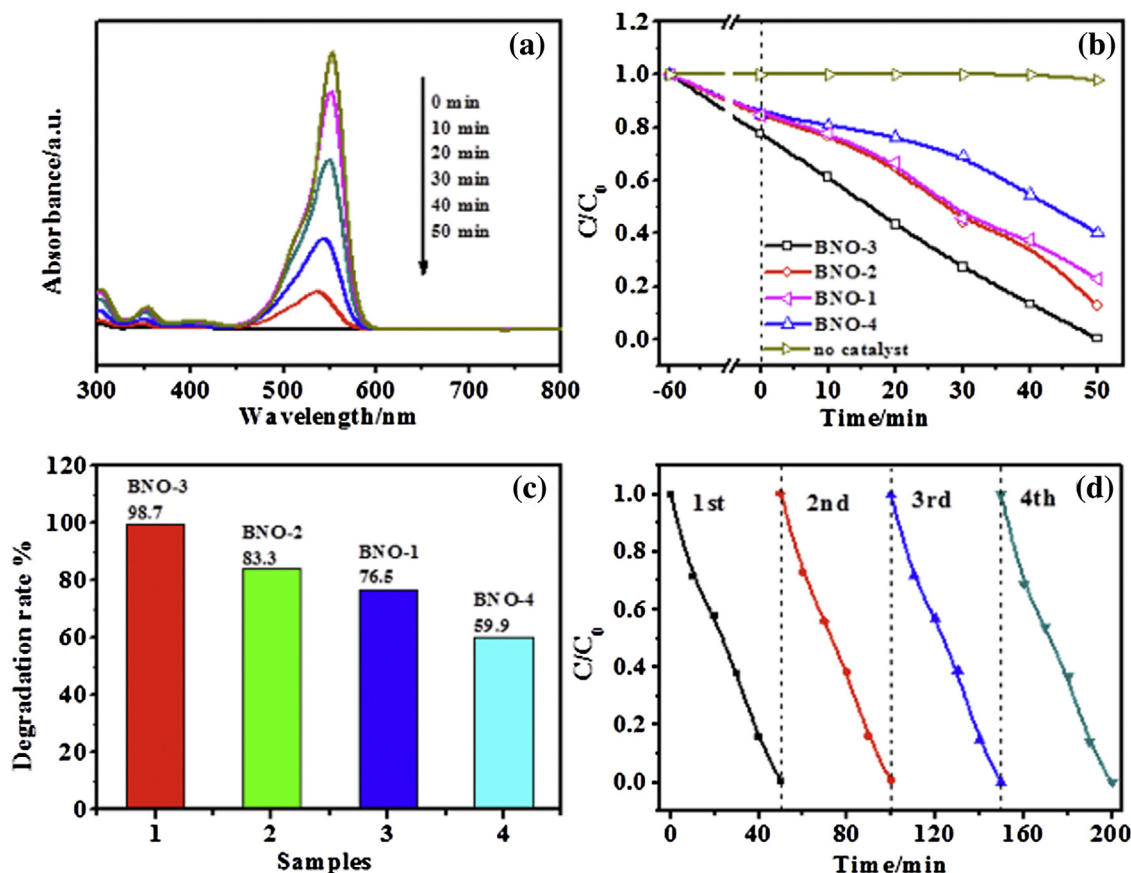
Fig. 8. Under visible light irradiation (a) The temporal evolution of the RhB absorption spectra in the existence of the Bi_3NbO_7 porous nanosheets (BNO-3), (b) photodegradation of RhB with different samples, (c) comparison of photodecomposition of RhB over different samples, (d) reuse of the Bi_3NbO_7 porous nanosheets (BNO-3).

oretical value of the angle between the (220) and (200) planes. A possible formation mechanism of porous Bi_3NbO_7 nanosheets was proposed. This cubic BNO-3 sample possess fluorite-type crystal structure constructed by hexahedal MO_7 units (M = Bi^{3+} or Nb^{5+}) [23,24]. There is one vacant position in the eight apexes of the hexahedral MO_7, which may provide sites for the formation of coordination bonds such as M—N and M—O between metallic atom and urea. During the nucleation of Bi_3NbO_7, with the presence of urea, various M—N and M—O bonds were formed. The metallic ions not only combined with HO^-, but also coordinated with O and N of urea. Then the M_4O_7 crystal nucleus with urea defects grew and generated sheet-like Bi_3NbO_7 nanostructures. Finally, the urea defects decomposed with the reaction temperature rising and reaction time extending, leading to the formation of porous Bi_3NbO_7 nanosheets.

3.3. BET analysis

The surface areas and porous structures of samples were further determined by nitrogen physical adsorption–desorption method. As to Bi_3NbO_7 porous nanosheets, the sample took on representative type IV isotherm with a distinct H_3 hysteresis loops in the range of 0.5–1.0 P/P_0, which was characteristic of porous materials [25], indicating well the existence of pores in the nanosheets (Fig. 5). Meanwhile, the above SEM images showed a distinct surface morphology of nanosheets and obvious pores, which was in favor of hysteresis loops isotherms. At relative pressures (P/P_0) approaching 1.0, the isotherm also showed adsorption, which demonstrated the formation of macropores [26]. The corresponding pore diameter distribution proved the existence of mesopores (2–50 nm) and

macropores (>50 nm, Fig. 5 inset). This hierarchical structure possessing both mesopores and macropores might act as high efficient transport paths between reactants and products in photocatalytic process [27]. The BET specific surface areas of these samples were presented as 9.7 m^2/g, 11.06 m^2/g and 16.47 m^2/g for BNO-1, BNO-2, and BNO-3 respectively. The BNO-3 sample had the largest BET surface which could be beneficial to the adsorption of the substrates. The remarkable structure of Bi_3NbO_7 porous nanosheets (BNO-3) might lead to higher photocatalytic activity than the non-porous ones.

3.4. Optical properties

The optical properties of semiconductor materials are very important in the photosensitization activity. Thus, the UV–vis absorption spectra of the BNO samples were measured by UV–vis diffuse reflectance spectroscopy in the wavelength ranging from 200 to 800 nm (Fig. 6). For crystalline semiconductors, the optical absorption near the band edge follows the formula [28] $\alpha h\upsilon = A(h\upsilon - Eg)^{n/2}$, where α, h, υ, A and Eg, represented absorption coefficient, Planck constant, light frequency, proportionality constant and band gap, respectively. Among them, n relies on the characteristics of the transition in a semiconductor, namely, direct transition ($n = 1$) or indirect transition ($n = 4$). In this experiment, the value of n for Bi_3NbO_7 nanosheets was evaluated to be 4. Through extrapolating the linear portion of the $(\alpha h\upsilon)^2$ versus $h\upsilon$ curves to the energy axis at $\alpha = 0$, the value of band gap of BNO-3 was estimated to be 2.6 eV, indicating the improvement of absorption ability [29], which might result in higher quantum efficiency of photocatalysis. With the increasing amount of urea content, there was
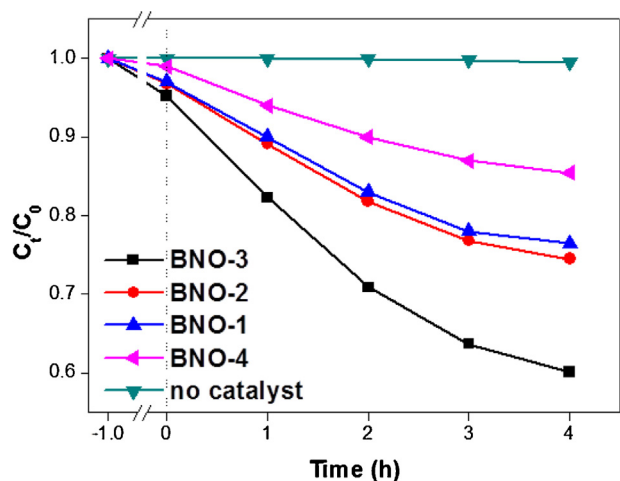
Fig. 9. Photodegradation of salicylic acid under visible light irradiation over different BNO samples.

Fig. 10. Photodegradation of RhB under visible light irradiation over BNO-5 and BNO-6 samples.

no significant difference of the absorbance of Bi_3NbO_7 nanosheets, corresponding band-gap value around 2.7 eV. The obvious difference of the band gap energies in Bi_3NbO_7 samples might be due to the changes of mesoporous and macropores conformation in the nanosheets. From our observation, Bi_3NbO_7 porous nanosheets (obtained at pH 13) had a narrow band gap, which could benefit photocatalytic reactions well. The main difference of BNO-3 and BNO-2/BNO-1 is that the various pores in BNO-3. BNO-1 has no pores and BNO-2 has very little pores. These pores would expose different edges, angles and facets from the single crystal nanosheet and these facets should be responsible for the shoulder peak in the DRS spectrum of BNO-3. Exposed facets possessing higher surface energy would lead to the red shift of the sample [30,31]. The porous structure of BNO-3 would expose some high energy facets which BNO-1 and BNO-2 do not have. These facets lead to the shoulder peak and smaller band gap of BNO-3 compared with BNO-1/BNO-2.

3.5. XPS spectra

In order to reveal the surface element compositions and the chemical states of the porous nanosheets, the as-prepared samples were measured by X-ray photoelectron spectroscopy (XPS). The XPS survey spectrum was shown in Fig. 7a, proving the existence of Nb, Bi, and O in the porous nanosheets. The C peak was mainly derived from the XPS instrument itself. No peaks from other impurities could be detected, indicating the high purity of the Bi_3NbO_7 surface. The Bi 4f region in the high-resolution XPS spectrum (Fig. 7b) was split into two individual peaks at 158.6 and 164.0 eV, which belonged to the binding energies of Bi $4f_{7/2}$ and Bi $4f_{5/2}$ respectively, indicating the chemical valence of bismuth element in the sample were tri-valence [32,33]. The lower binding energies peaks at 157.4 and 162.7 eV suggested the possibility appearance of $Bi^{(+3-x)}$ at the surface of Bi_3NbO_7 porous nanosheets, which might attribute to a deficiency in oxygen and an enhanced concentration of oxygen vacancies in the vicinity, leading to the higher quantum efficiency in the photocatalytic process [34]. The Nb $3d_{5/2}$ and Nb $3d_{3/2}$ peaks were assigned to the binding energy at 208.9 and 206.2 eV, respectively (Fig. 7c), which was well matched with the Nb^{+5} oxidation state [35]. The O 1s peak was fitted by one peak at 529.3 eV (Fig. 7d). By XPS surface elemental analysis, relative atomic ratio of Nb/Bi of as-prepared nanosheets (BNO-3) was detected as 3.02, which was close to ideal reactant mole ratio. Based on the XRD, TEM and XPS, it could be confirmed that single and pure-phase Bi_3NbO_7 single crystal porous nanosheets was synthesized successfully.
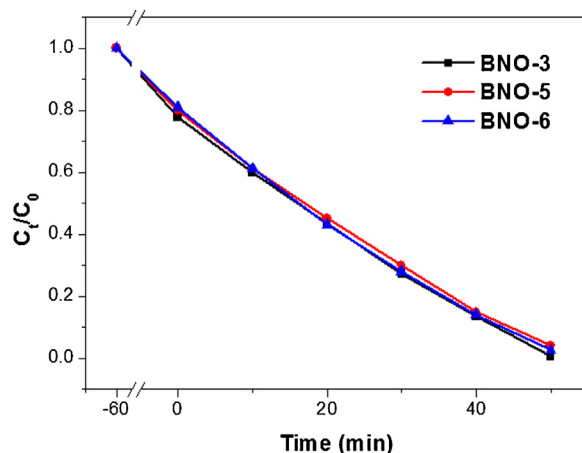
3.6. Photocatalytic activity

The photocatalytic degradation of dyes solutions chosen as model pollutants is widely used to evaluate the activity of photocatalysts. The photocatalytic activity of Bi_3NbO_7 porous nanosheets was characterized under visible light using Rhodamine-B (RhB). The characteristic absorption peak of RhB is located at 553 nm. As the irradiation time went on, the peak declined promptly and disappeared after 50 min when BNO-3 was chosen as the photocatalyst. With the diminishment of the peak at 553 nm, the peaks around at 354 and 306 nm also decreased gradually (Fig. 8a), which suggested that it was a mineralization process accompanying the destruction of the conjugated structure of RhB [36]. Photodegradation efficiencies of RhB with different as-obtained samples under visible light were observed in Fig. 8b. Degradation of RhB could hardly happen in the absence of photocatalyst under visible-light illumination. However, when the catalysts were added into the reaction system, RhB vanished within 50 min, indicating the removal of RhB was mainly owing to photocatalysis (Fig. 8b). Under visible light irradiation for 50 min, the degraded percentages of RhB were estimated to be 59.9, 76.5, 83.3 and 98.7 for BNO-4, BNO-1, BNO-2, and BNO-3 (Fig. 8c). Apparently, the Bi_3NbO_7 porous nanosheets (BNO-3) exhibited higher activity for the RhB degradation than both nonporous and bulk ones under visible light irradiation. It could be seen that importing more urea content and incorporated base quantity could improve the photocatalytic capacity. Evidently, among all tested samples, BNO-3 performed the highest photocatalytic activity. Many factors could affect the photocatalytic activity, where they might cooperate with each other and better promote the photocatalytic activity. In this experiment, comparing with the nonporous and bulk BNO samples, the higher photocatalytic efficiency of BNO-3 might due to narrow band gap, larger specific surface area which could provide much more active sites, promote photo-generated holes consumption and strengthen photo-generated electrons harvest. This novel porous structure hierarchical structure possessing various pores might act as high efficient transport paths between reactants and products in photocatalytic process. As we know, RhB could be sensitized by visible light. In order to confirm the visible light photocatalytic property of BNO samples, a colorless organic molecule, salicylic acid (5 mg/L, 50 mL) was chosen to test the photocatalytic performance of the samples under visible light irradiation. The results shown in Fig. 9 exhibits that these BNO samples possessed good photocatalytic property for degradation of salicylic acid. Among these samples, BNO-3 (Bi_3NbO_7 porous nanosheets) was a better photocatalyst than the other samples.
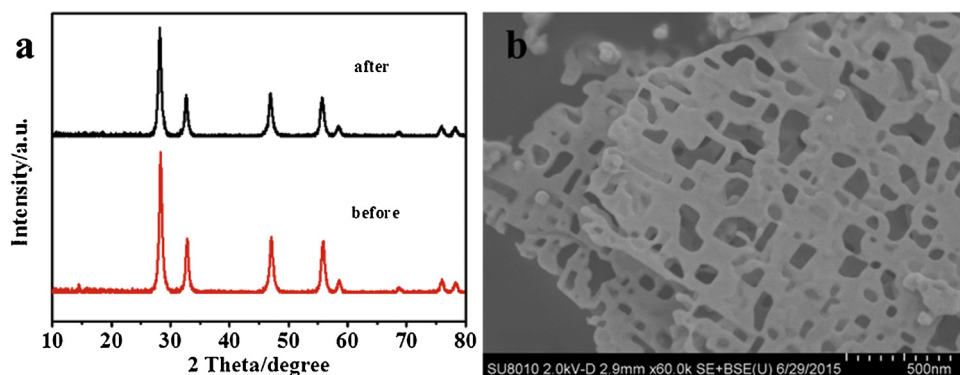
Fig. 11. XRD pattern and SEM image of BNO-3 after photocatalytic reactions, (a) XRD patterns of BNO-3 before and after photocatalytic reaction, (b) SEM images of BNO-3 after four batches of photodegradation.

In this experiment, the BET specific surface areas as well as the photocatalytic performance of these samples increase with the increase amount of the urea. To investigate the effect of higher urea content on these properties, samples with 2.52 g and 3.36 g urea added in the synthesis process respectively (marked as BNO-5 and BNO-6) were prepared. The BET special surface areas of BNO-5 and BNO-6 were 15.98 and 16.35 m^2/g, respectively. The results were almost the same with BNO-3. Photocatalytic performance of the two samples was tested through the photodegradation of RhB under the same condition of the reaction by BNO-3. The RhB could be decomposed within one hour, indicating the photocatalytic activity of these two samples was no higher than that of BNO-3 (Fig. 10). Thus, the urea content of 1.68 g added in the synthesis process (BNO-3) could obtain single crystal Bi_3NbO_7 porous nanosheets with good photocatalytic activity.

To test the stability of porous Bi_3NbO_7 nanosheets, the photocatalyst (BNO-3) for the RhB photodegradation was reused four times, shown in Fig. 8d. It could be seen that no obvious deactivation occurred over Bi_3NbO_7 porous nanosheets used for the RhB photodegradation under visible light irradiation. XRD pattern (Fig. 9a) and SEM images (Fig. 9b) of Bi_3NbO_7 porous nanosheets photocatalyst (BNO-3) after four recycles was also obtained. The main position and proportion of the peaks were nearly consistent with newly prepared samples, and the morphology of the reused samples did not change, certifying high stability (Fig. 11). Therefore, these Bi_3NbO_7 porous nanosheets can serve as an attractive and enduring photocatalyst (Fig. 11).

4. Conclusions

In summary, Bi_3NbO_7 single crystalline nanosheets had been successfully synthesized by a simple and direct solvothermal route. Crystallinity and morphology structure of Bi_3NbO_7 nanosheets could be effectively controlled by tuning urea content and incorporated potassium hydroxide solution studied systematically. Without the addition of potassium hydroxide solution to regulate the pH value, only Bi_3NbO_7 nonporous nanosheets could be obtained, possessing lower crystallinity. Introduction of potassium hydroxide solution, especially the sample obtained at pH value 13 appeared numerous pores in the Bi_3NbO_7 nanosheets, enhancing their crystallinity. Interestingly, the pores always had at least one right angle and for one individual nanosheet, the two edges of the right angle were always parallel to each other respectively. These Bi_3NbO_7 novel porous nanosheets possessed the highest photocatalytic activity for both RhB and salicylic acid degradation under visible light irradiation than nonporous and bulk ones, which might attribute to narrower band gaps, novel porous architecture, the

larger specific surface area and considerable oxygen vacancies. Moreover, the sample could be reused for 4 times with no deactivation and morphology change. This work provides a facile and simple method to synthesize novel porous BNO nanosheet as potential remarkable photocatalytic activity in visible light spectral range.

References

[1] T. Zhou, J. Hu, Environ. Sci. Technol. 44 (2010) 8698–8703.
[2] H. Wang, L. Zhang, Z. Chen, J. Hu, S. Li, Z. Wang, J. Liu, X. Wang, Chem. Soc. Rev. 43 (2014) 5234–5244.
[3] L. Ding, H. Chen, Q. Wang, T. Zhou, Q. Jiang, Y. Yuan, J. Li, J. JL, J.C. Hu, Chem. Commun. 5 (2016) 994–997.
[4] T. Zhou, W. Pang, C. Zhang, J. Yang, Z. Chen, H. Liu, Z. Guo, ACS Nano 8 (2014) 8323–8333.
[5] W. Fang, Z. Huo, P. Liu, X. Wang, M. Zhang, Y. Jia, H. Zhang, H. Zhao, H. Yang, X. Yao, Chem. Eur. J. 20 (2014) 11439–11444.
[6] Y. Sun, H. Cheng, S. Gao, Z. Sun, Q. Liu, Q. Liu, F. Lei, T. Yao, J. He, S. Wei, Y. Xie, Angew. Chem. Int. Ed. 51 (2012) 8727–8731.
[7] M. Luo, Y. Liu, J. Hu, H. Liu, J. Li, ACS Appl. Mater. Interfaces 4 (2012) 1813–1821.
[8] X. Xiong, L. Ding, Q. Wang, Y. Li, Q. Jiang, J. Hu, Appl. Catal. B Environ. 188 (2016) 283–291.
[9] P. Pathak, M. Meziani, Y. Li, L. Cureton, Y. Sun, Chem. Commun. (2006) 1234–1235.
[10] Z. Zou, J. Ye, K. Sayama, H. Arakawa, Nature 414 (2001) 625–627.
[11] X. Chen, S. Shen, L. Guo, S. Mao, Chem. Rev. 110 (2010) 6503–6570.
[12] A. Fujishima, K. Honda, Nature 238 (1972) 37–38.
[13] R. Chong, J. Li, X. Zhou, Y. Ma, J. Yang, L. Huang, H. Han, F. Zhang, C. Li, Chem. Commun. 50 (2014) 165–167.
[14] X. Chen, C. Burda, J. Am. Chem. Soc. 130 (2008) 5018–5019.
[15] Z. Liu, G. Ji, D. Guan, B. Wang, X. Wu, J. Colloid Interface Sci. 457 (2015) 1–8.
[16] Y. Liu, L. Chen, J. Hu, J. Li, R. Richards, J. Phys. Chem. C 114 (2010) 1641–1645.
[17] T. Shibata, G. Takanashi, T. Nakamura, K. Fukuda, Y. Ebina, T. Sasaki, Energy Environ. Sci. 4 (2011) 535–542.
[18] L. Zhang, W. Wang, L. Zhou, H. Xu, Small 3 (2007) 1618–1625.
[19] L. Zhou, W. Wang, S. Liu, L. Zhang, H. Xu, W. Zhu, J. Mol. Catal. A Chem. 252 (2006) 120–124.
[20] Y. Shimodaira, H. Kato, H. Kobayashi, A. Kudo, J. Phys. Chem. B 110 (2006) 17790–17797.
[21] J. Jiang, M. Wang, Q. Chen, S. Shen, M. Li, L. Guo, RSC Adv. 4 (2014) 10542–10548.
[22] G. Zhang, J. Yang, S. Zhang, Q. Xiong, B. Huang, J. Wang, W. Gong, J. Hazard. Mater. 172 (2009) 986–992.
[23] L. Wang, W. Wang, M. Shang, S. Sun, W. Yin, J. Ren, J. Zhou, J. Mater. Chem. 20 (2010) 8405–8410.
[24] A. Castro, E. Aguado, J. Rojo, P. Herrero, R. Enjalbert, J. Galy, Mater. Res. Bull. 33 (1998) 31–41.
[25] J. Xia, S. Yin, H. Li, H. Xu, Y. Yan, Q. Zhang, Langmuir 27 (2011) 1200–1206.
[26] Y. Shen, Q. Wei, W. Guo, L. Fan, D. Liu, S. Li, J. Alloys Compd. 618 (2015) 311–317.
[27] A. Castro, E. Aguado, J. Rojo, P. Herrero, R. Enjalbert, J. Galy, Mater. Res. Bull. 33 (1998) 31–41.

[28] S. Zhang, G. Zhang, S. Yu, X. Chen, X. Zhang, J. Phys. Chem. C 113 (2009) 20029–20035.
[29] J. Fang, J. Ma, Y. Sun, Z. Liu, C. Gao, Solid State Sci. 13 (2011) 1649–1653.
[30] Y. Bi, S. Ouyang, N. Umezawa, J. Cao, J. Ye, J. Am. Chem. Soc. 133 (2011) 6490–6492.
[31] J. Jiang, K. Zhao, X. Xiao, L. Zhang, J. Am. Chem. Soc. 134 (2012) 4473–4476.
[32] J. Jiang, L. Zhang, H. Li, W. He, J. Yin, Nanoscale 5 (2013) 10573–10581.
[33] Y. Yu, C. Cao, H. Liu, P. Li, F. Wei, Y. Jiang, W. Song, J. Mater. Chem. A 2 (2014) 1677–1681.

[34] L. Ding, R. Wei, H. Chen, J. Hu, J. Li, Appl. Catal. B Environ. 172–173 (2015) 91–99.
[35] W. Wu, S. Liang, L. Shen, Z. Ding, H. Zheng, W. Su, L. Wu, J. Alloys Compd. 520 (2012) 213–219.
[36] J. Hu, W. Fan, W. Ye, C. Huang, X. Qiu, Appl. Catal. B Environ. 158–159 (2014) 182–189.